

Supporting Information

Covalently linked dual network achieved by rapid grafting of poly(p-phenylenediamine) -phosphomolybdic acid on reduced graphene oxide aerogel for improving performance of supercapacitor

Jing Gao,^{‡,*} Mingxing Tong,[‡] Zhengyang Xing, Qiuyang Jin, Junxi Zhou, Lihui Chen, Haolan Xu and Guohua Li*

1 Synthesis of samples

1.1 Synthesis of GO

Graphene oxide was prepared from natural graphite flakes via modified Hummer's method. Briefly, 1.5 g of graphite flakes was added to a mixture of concentrated sulfuric acid (180 mL) and phosphoric acid (20 mL) under stirring at 0 °C. Then, potassium permanganate (9.0 g) was added slowly to keep the temperature of the suspension lower than 20 °C. Subsequently, the reaction temperature was heated to 35 °C and kept in water bath for about 0.5 h. Then, the reaction system was kept at 50 °C for approximately 12 h. After that 200 mL of water was added followed by a slow addition of 20 mL of H₂O₂ (30%). The solution then turned from brown to yellow, which was filtered and washed with HCl aqueous solution (10 %) and deionized water, respectively. Finally, the solution was dispersed by ultrasonication for 2 h to form a GO aqueous suspension.

1.2 Synthesis of PPD-PMo₁₂@rGO

PMo₁₂ (0.05 g, 0.027mmol) was dissolved in deionized water (1 mL) at room temperature under stirring, to which p-phenylenediamine (p-PD) (0.027 g, 0.25 mmol) dissolved in deionized water (2 mL) was slowly dropped in. GO dispersion solution (3 mL, 5 mg mL⁻¹) was then added into the above mixture, leading to hydrogel within 1 min. After being washed with deionized water, the hydrogel was freezing dried and transformed into PPD-PMo₁₂@rGO aerogel.

1.3 Synthesis of PPD-PMo₁₂

PMo₁₂ (0.05 g, 0.027mmol) was dissolved in deionized water (1 mL) at room temperature under stirring, to which p-PD (0.027 g, 0.25 mmol) dissolved in deionized water (2 mL) was slowly dropped in, which produced a suspension. The suspension was washed by deionized water and ethanol for several times, centrifuged and then dried at 80 °C for 6 h, leading to PPD-PMo₁₂.

1.4 Synthesis of PMo₁₂@GO

PMo₁₂ (0.05 g, 0.027mmol) was dissolved in deionized water (2 mL) at room temperature under stirring, to which GO suspension (3 mL, 5 mg mL⁻¹) was added in. After being stirred for 30 min, the mixture was freezing dried to obtain PMo₁₂@GO.

1.5 Synthesis of p-PD@GO

Procedures to prepare p-PD@GO were similar to that of PMo₁₂@GO except that PMo₁₂ was replaced by p-PD (0.027 g).

1.6 Synthesis of PPD-PMo₁₂+rGO

GO was first reduced by ascorbic acid at 80°C for 2h to obtain rGO, which was then physically mixed with PPD-PMo₁₂ to obtain PPD-PMo₁₂+rGO.

2 Characterizations of samples

Field emission scanning electron microscopy (FESEM) was performed on a HITACHI S-4700 (Hitachi). In order to obtain TEM and STEM images, the samples were first dispersed in ethanol solution and then ultrasounded for 15 min. A small drop of the dispersion was evaporated on surface of a carbon support film supported by a Cu mesh. TEM/STEM images were obtained by using a transmission electron microscope (TEM) (Tecnai G2 F30 S-Twin, Philips-FEI, Netherlands) at an acceleration voltage of 300 kV. Elemental distribution was studied using energy dispersive X-ray spectroscopy (EDS) on a Tecnai G2 F30 equipped with an Oxford/INCA EDS. Thermogravimetric (TG) measurements were carried out from a TG instrument (STA-449F3, NETZSCH) with heating rate of 5°C min⁻¹ in flowing oxygen. The specific surface area, pore size, and pore volume were determined by a Brunauer-Emmett-Teller (BET) apparatus, ASAP2020 (Micromeritics, US). XRD patterns were collected using an X'Pert PRO (PANalytical) with a high-intensity Cu K α irradiation ($\lambda = 1.54 \text{ \AA}$). Raman spectra were recorded by using a LabRAM HR800 (Horiba JobinYvon) with a 531.95 nm laser. The Fourier transform infrared (FT-IR) spectrums were investigated by a FT-IR spectrometer (Nicolet 6700). XPS results were recorded with an ESCALab220i-XL (Thermofisher, Co., Ltd., England). Electronic conductivity measurements were carried out from a ST2255 type high resistance meter with ST2722-SD model by using four-probe method.

3 Measurements of Electrochemical Performances

All the electrochemical experiments were conducted on a CHI 660E electrochemistry workstation. The working electrode, composed of a slurry of active materials (75 wt%), carbon black (15 wt%) and polyvinylidene fluoride (PVDF, 10 wt%) dissolved in N-methyl-2-pyrrolidinone, was coated onto carbon paper ($\sim 1 \text{ mg cm}^{-2}$) and then dried at $80 \text{ }^\circ\text{C}$ overnight in an oven. A platinum foil ($1 \times 1 \text{ cm}^2$) and an Ag/AgCl (3 M KCl) electrode were used as the counter electrode and the reference electrode, respectively. The working electrode was tested by cyclic voltammetry (CV) and galvanostatic charge/discharge (GCD) in 1 M H_2SO_4 as electrolyte. EIS measurement was performed at open circuit potential a sinusoidal signal in a frequency range from 100 kHz to 10 mHz at an amplitude of 5 mV. A cycling test was performed using GCD measurements at a current density of 20 A g^{-1} for 30000 cycles. The gravimetric specific capacitance derived from the cyclic voltammetry curves was calculated based on the following equation:

$$C_s = \frac{\int_0^{v/s} |j| dt}{V} \quad (1)$$

where C is the gravimetric capacitance (F g^{-1}), j is the gravimetric current density (A g^{-1}), s is the scan rate (V s^{-1}), and V is the potential window (V).

4. Diffusion mechanism

The relationship between current and potential sweep rate has been examined extensively.²
³ The diffusion mechanism analysis shows that the currents in the CV tests are directly proportional to the scan rate, which obeys the equation:

$$i = a\nu^b \quad (2)$$

where i is current, a and b are the adjustable parameters, ν is the scan rate. b value close to 1 indicates the charge storage kinetics is dominated by surface-controlled mechanism, while b value close to 0.5 suggests the charge storage kinetics is dominated by diffusion-controlled mechanism.

5. Capacitance contribution of surface-control and diffusion-control

The current response (i) at a fixed potential (V) can be described as the combination of two separate mechanisms, namely capacitive effects ($k_1 \nu$) and diffusion-controlled insertion ($k_2 \nu^{0.5}$). The Dunn's method⁴⁻⁶ was used to investigate the charge storage contributions from the capacitive-controlled process and the diffusion-controlled process according to equation:

$$i(V) = k_1 \nu + k_2 \nu^{0.5} \quad (3)$$

where ν is the scan rate, k_1 and k_2 are proportionality constants related to the capacitive and diffusion-limited processes, by determining both k_1 and k_2 , it could distinguish the capacitive and diffusion capacitance, respectively.

Table S1 Comparisons of preparations of graphene-based hydrogels under different conditions.

No.	Reactants	Temp.	Formation time	Shape	Ref.
1	GO + peptides	RT	12 h	Irregular	[7]
2	GO + poly(vinyl alcohol)	RT	20 min	Irregular	[8]
3	GO + Fe-MOF crystals	RT	Several mins	Irregular	[9]
4	GO + PPy	RT	3 days	Cylinder	[10]
5	GO + aniline	RT	24 h	Sphere	[11]
6	GO + V ₂ O ₅ + thiourea	RT	20 min	Cylinder	[12]
7	GO + (NH ₄) ₂ S ₂ O ₈ + phytic acid + aniline	4 °C	Several mins	Irregular	[13]
8	GO + polymer latex + ascorbic acid	60 °C	2 h.	Cylinder	[14]
9	GO + resorcinol + HCHO + Na ₂ CO ₃ + Ag	85 °C	3 days	Cylinder	[15]
10	GO + PANI	90 °C	2 h	Cylinder	[16]
11	GO + (NH ₄) ₂ S	95°C	3 h	Cylinder	[17]
12	GO + PPD + PMo₁₂	RT	Within 1 min	Cylinder	This work

Table S2 FTIR data analysis of GO, PPD-PMo₁₂ and PPD-PMo₁₂@rGO aerogel samples.

Characteristic vibration	Wavenumbers (cm ⁻¹)	Samples
$\nu_{\text{C=O}}$ (carboxyl)	1737	GO
$\nu_{\text{C=O}}$ (amide)	1630	PPD-PMo ₁₂ @rGO
$\nu_{\text{C=C}}$ (aromatic)	1608	GO
$\beta_{\text{N-H}}$ (symmetry)	1503	PPD-PMo ₁₂ , PPD-PMo ₁₂ @rGO
$\nu_{\text{C-N}}$ (amide)	1395	PPD-PMo ₁₂ @rGO
$\nu_{\text{C-OH}}$	1380	GO
$\nu_{\text{C-N}}$ (primary amine)	1262	PPD-PMo ₁₂
$\nu_{\text{C-O-C}}$	1225	GO
$\nu_{\text{C-N}}$ (N ⁺)	1168	PPD-PMo ₁₂ @rGO
$\nu_{\text{P-O}}$	1067	PPD-PMo ₁₂ , PPD-PMo ₁₂ @rGO
$\nu_{\text{C-O-C}}$ (epoxide)	1048	GO
$\nu_{\text{Mo=O}}$	947	PPD-PMo ₁₂ , PPD-PMo ₁₂ @rGO
$\nu_{\text{Mo-O-Mo}}$	895	PPD-PMo ₁₂ , PPD-PMo ₁₂ @rGO

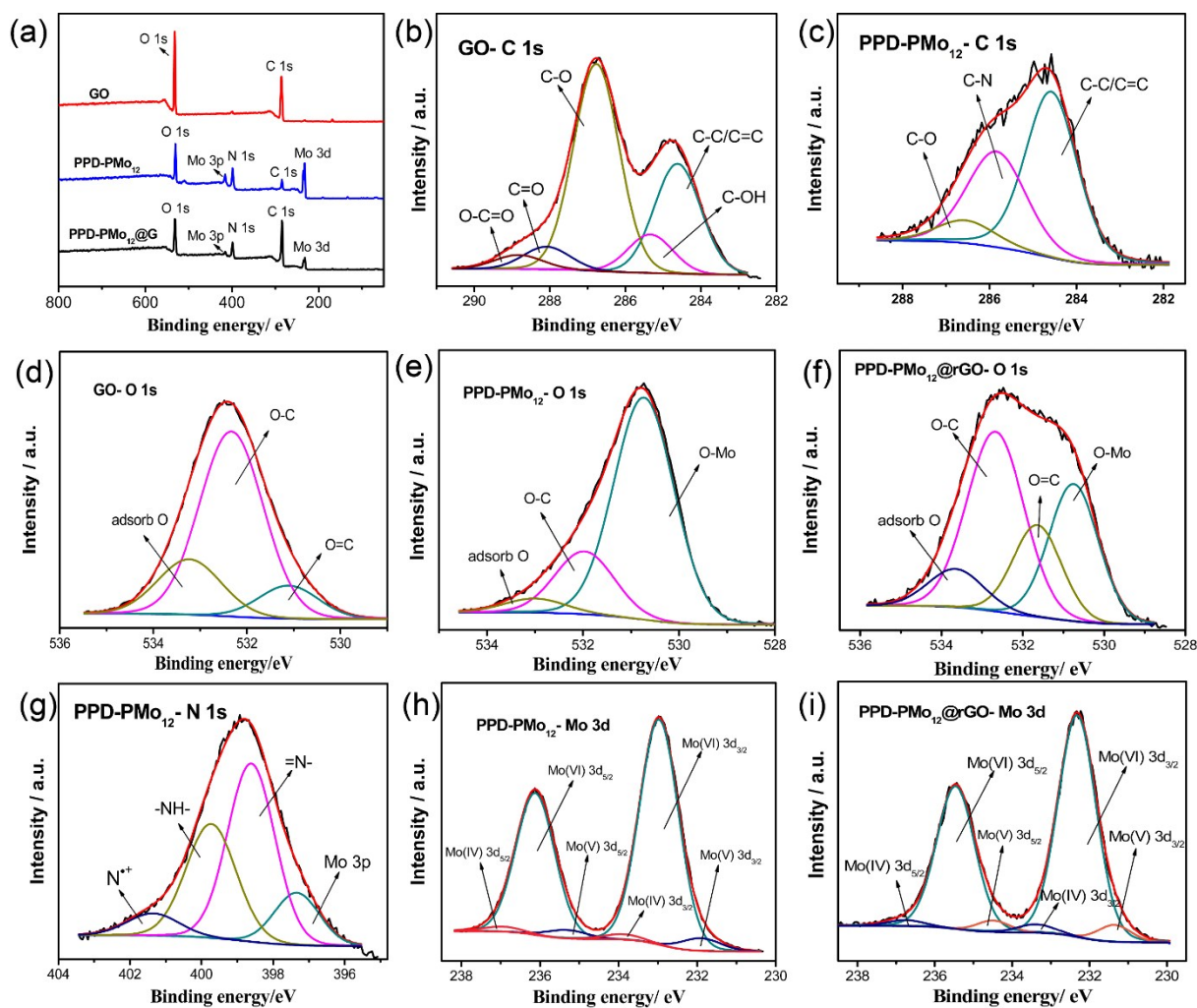


Fig. S1. (a) Full-scan XPS spectra of the samples; C 1s spectra of (b) GO and (c) PPD-PMo₁₂; O 1s spectra of (d) GO, (e) PPD-PMo₁₂ and (f) PPD-PMo₁₂@rGO aerogel; (g) N 1s spectra of PPD-PMo₁₂; Mo 3d spectra of (h) PPD-PMo₁₂ and (i) PPD-PMo₁₂@rGO aerogel.

Table S3 XPS data analysis of GO, PPD-PMo₁₂ and PPD-PMo₁₂@rGO aerogel samples.

a. C 1s data of the samples

Samples	C-C/C=C (eV)	C-N (eV)	C-OH (eV)	C-O (eV)	C=O (eV)	HN-C=O (eV)	O-C=O (eV)
GO	284.6		285.3	287.0	288.1		288.8
PPD-PMo ₁₂	284.6	285.5		286.6			
PPD-PMo ₁₂ @rGO	284.6	285.4		286.4	287.0	288.3	288.9

b. N 1s data of the samples

Samples	=N- (eV)	-NH-(eV)	-(O)C-NH- (eV)	-N ⁺ (eV)
PPD-PMo ₁₂	398.6	399.9		401.4
PPD-PMo ₁₂ @rGO	398.5	399.5	400.6	401.5

c. O 1s data of the samples

Samples	O-Mo (eV)	O=C (eV)	O-C (eV)	Adsorb O (eV)
GO		531.1	532.4	533.4
PPD-PMo ₁₂	530.6		532.2	533.1
PPD-PMo ₁₂ @rGO	530.6	531.6	532.7	533.6

d. Mo 3d data of the samples

Samples	Mo(V) 3d _{5/2} (eV)	Mo(V) 3d _{3/2} (eV)	Mo(VI) 3d _{5/2} (eV)	Mo(VI) 3d _{3/2} (eV)	Mo(IV) 3d _{5/2} (eV)	Mo(IV) 3d _{3/2} (eV)
PPD-PMo ₁₂	231.9	235.2	233.0	236.1	233.9	237.0
PPD-PMo ₁₂ @rGO	231.7	234.9	232.6	235.8	233.7	237.1

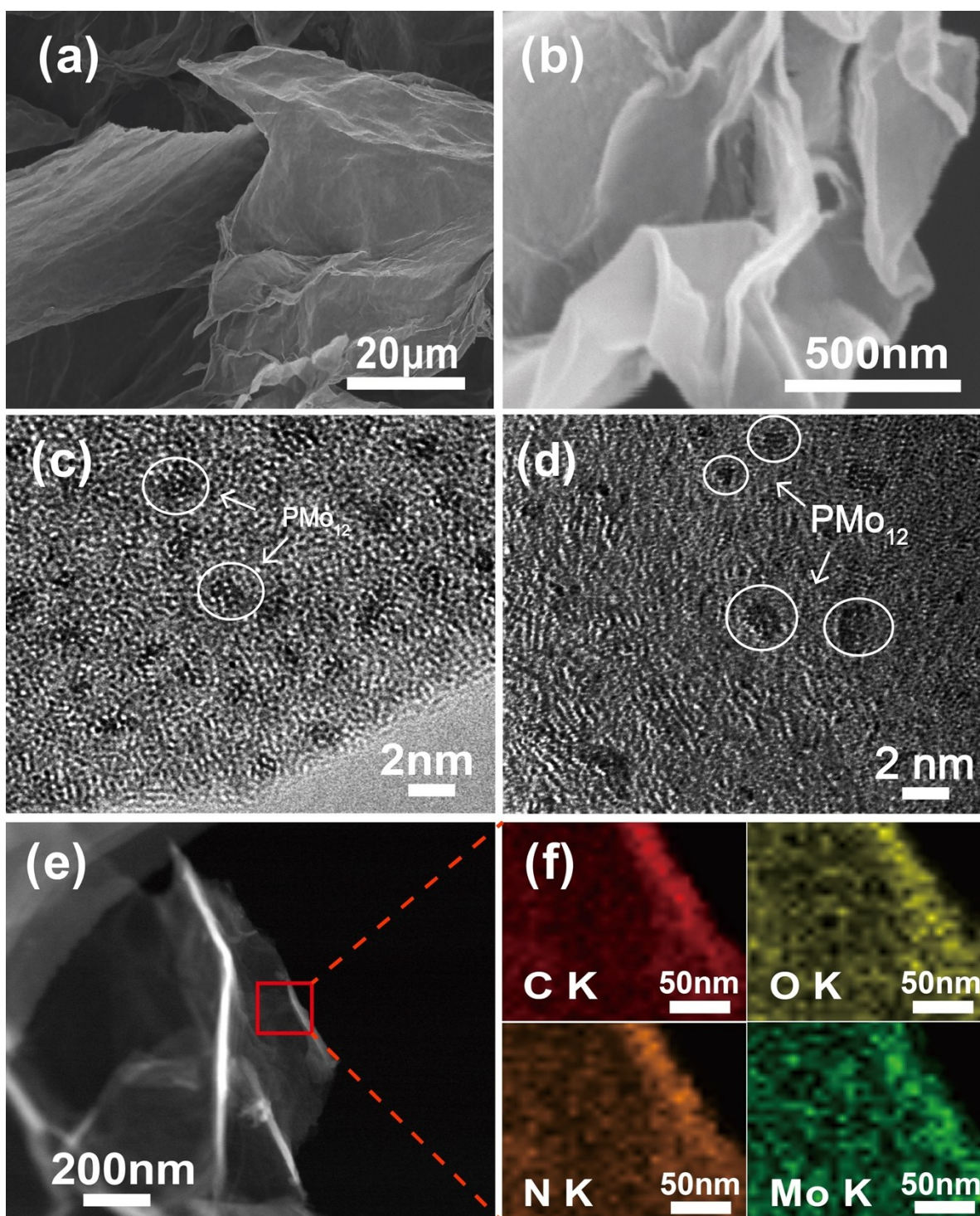


Fig. S2. SEM image of (a) GO and (b) PPD-PMo₁₂@rGO; HRTEM image of (c) PPD-PMo₁₂ and (d) PPD-PMo₁₂@rGO; (e) STEM image and (f) elemental mapping images of PPD-PMo₁₂@rGO obtained from a small region of Fig. S2e (red square).

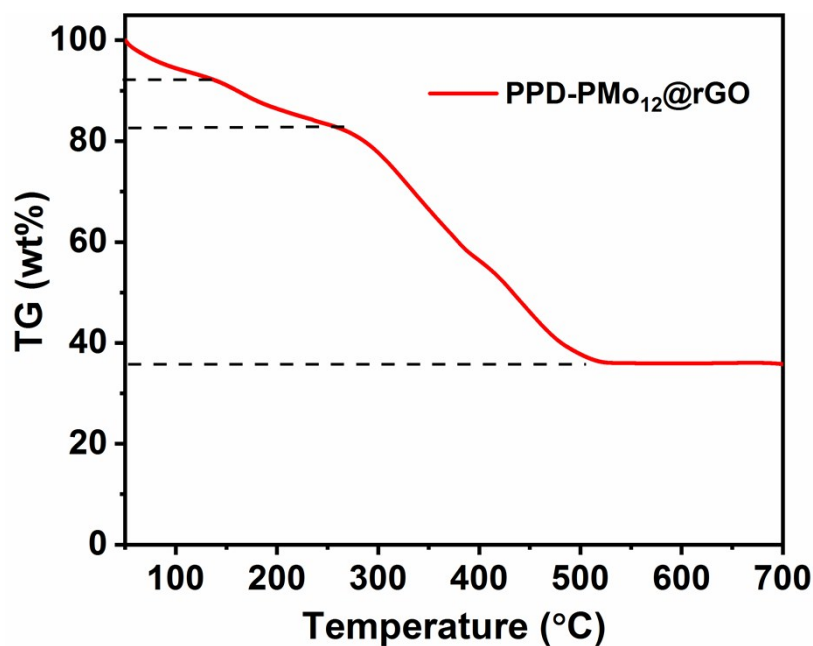


Fig. S3 TG curve of the PPD-PMo₁₂@rGO aerogel at a heating rate of 5 °C min⁻¹ in O₂.

Thermogravimetric (TG) test of PPD-PMo₁₂@rGO aerogel was carried out in oxygen and the results are presented in Fig. S3. Three successive process of weight loss can be observed in range of 50-110 °C, 120-270 °C and 280-560 °C, respectively, which could be ascribed to loss of absorbed water and decomposition of PPD, PMo₁₂ and rGO. After the three successive process of weight loss, the obtained product was MoO₃ (From 750 °C to 850 °C, the whole weight loss achieved to 100% due to sublimation of MoO₃, of which the melting point is 795 °C. Therefore, only weight loss before 700 °C is considered). Based on the weight of MoO₃, the weight percentage of PMo₁₂ in PPD-PMo₁₂@rGO aerogel could be calculated, which is about 38%. However, since both PPD and rGO have carbon elements and the molecular weight of PPD is unknown, so we can hardly obtain accurate composition of the PPD-PMo₁₂@rGO.

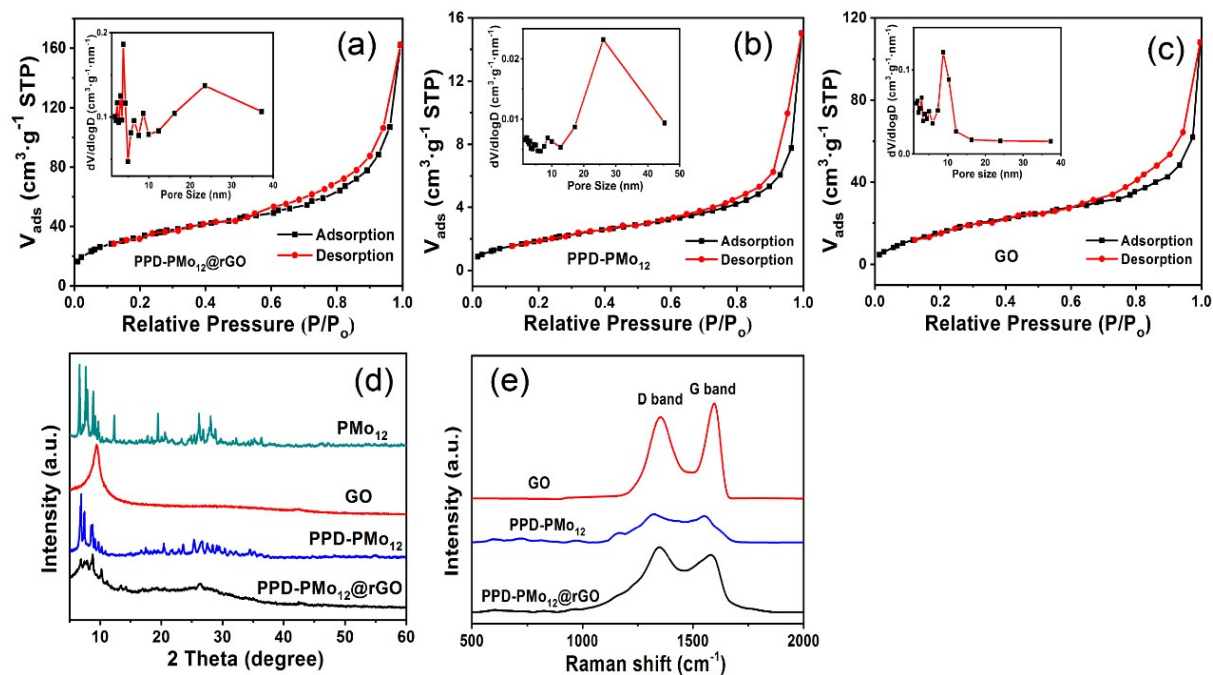


Fig. S4. N_2 adsorption/desorption isotherms and pore size distribution curves (the insets) of (a) PPD- $PMo_{12}@rGO$ aerogel and (b) PPD- PMo_{12} and (c) GO; (d) XRD patterns of PMo_{12} , GO, PPD- PMo_{12} and PPD- $PMo_{12}@rGO$; (e) Raman spectra of GO, PPD- PMo_{12} and PPD- $PMo_{12}@rGO$.

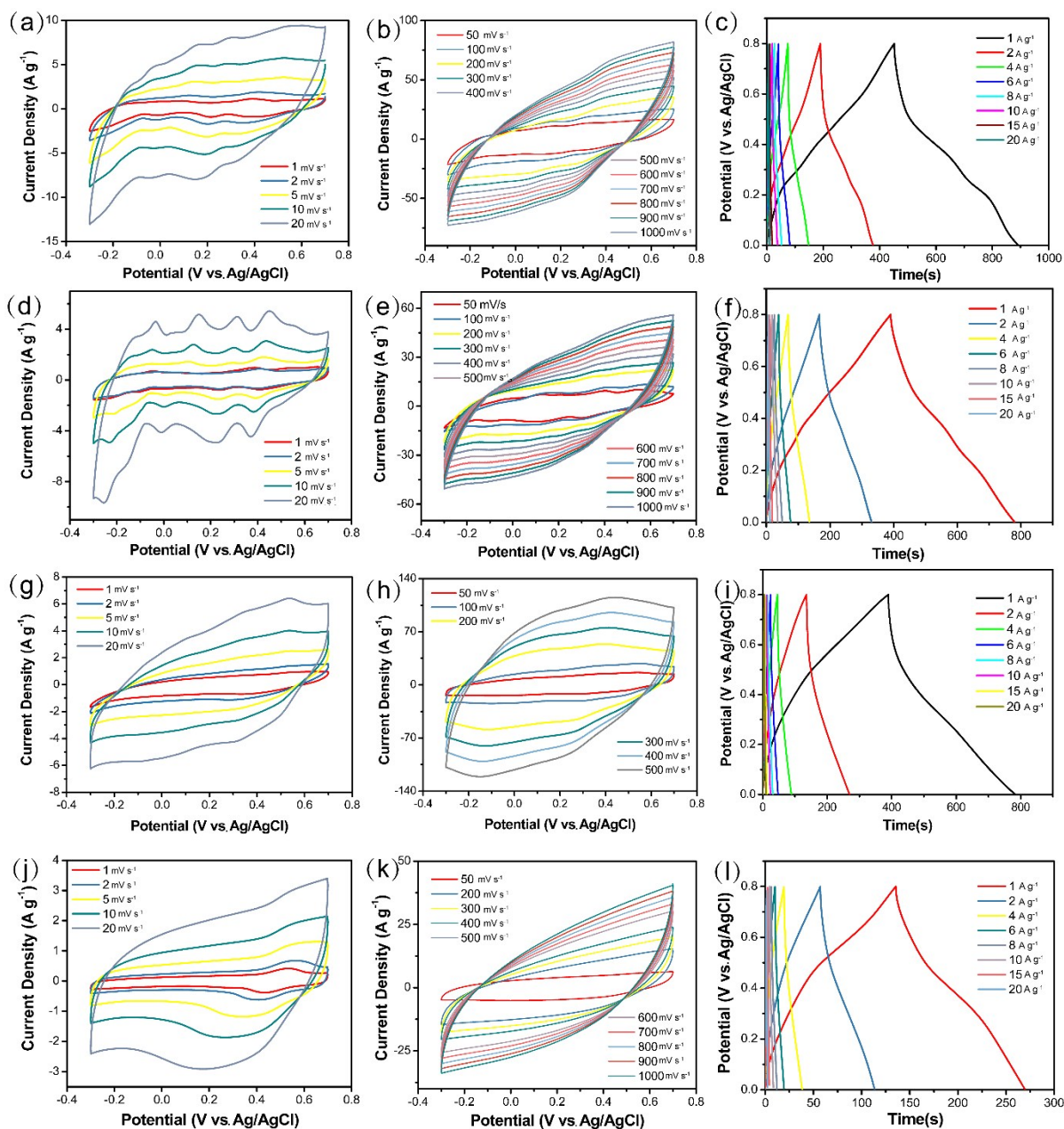


Fig. S5. (a, b) CV and (c) GCD curves of PPD-PMO₁₂; (d, e) CV and (f) GCD curves of PMO₁₂@GO; (g, h) CV and (i) GCD curves of PPD@GO; (j, k) CV and (l) GCD curves of GO.

The CV of PMO₁₂@GO shows many pairs of redox peaks. These peaks could be attributed the redox behavior of PMO₁₂. The PMO₁₂, which has strong oxidative ability in acid form, is a kind of redox compound and shows redox peaks in its CV curves. In this case, the

sample is $\text{PMo}_{12}@r\text{GO}$ obtained by physically mixing PMo_{12} and rGO. Since it is well known that rGO is a classical double-layer capacitive material that shows nearly no redox peaks in its CV curves, thus it can be concluded that the redox peaks can be ascribed to PMo_{12} .

Table S4 Capacitive performances of different samples.

Samples	Specific capacitance (F g^{-1}) at 1 mV s^{-1}	Specific capacitance (F g^{-1}) at 100 mV s^{-1}	Rate capability (%)
PPD- $\text{PMo}_{12}@r\text{GO}$	790	330	41.7
PPD- PMo_{12}	550	160	29.1
$\text{PMo}_{12}@r\text{GO}$	305	150	49.2
p-PD@GO	500	172	34.4
GO	195	75	38.4

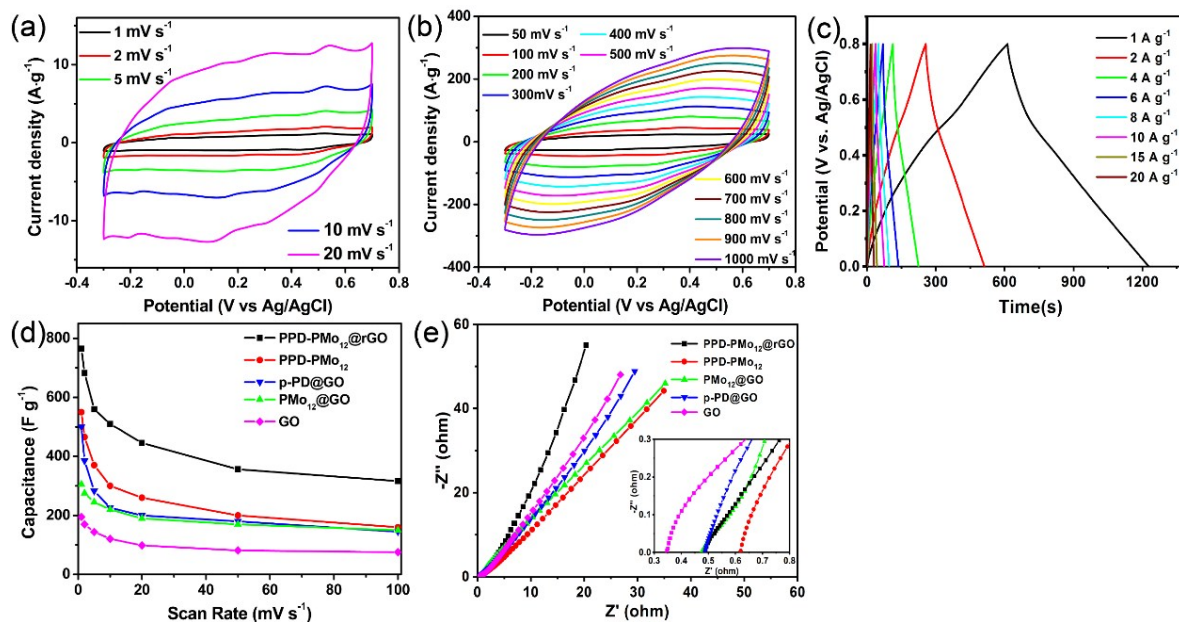


Fig. S6 (a, b) CV curves under different scan rates and (c) GCD curves under different current densities of the PPD- $\text{PMo}_{12}@r\text{GO}$ aerogel electrode; (d) Rate capability and (e) Nyquist plots of the samples.

Notably, the shape of the CV curve still show no significant deformation even when the scan rate was as high as 1000 mV s^{-1} , indicating an excellent capacitive behavior and a quick charge propagation capacity.

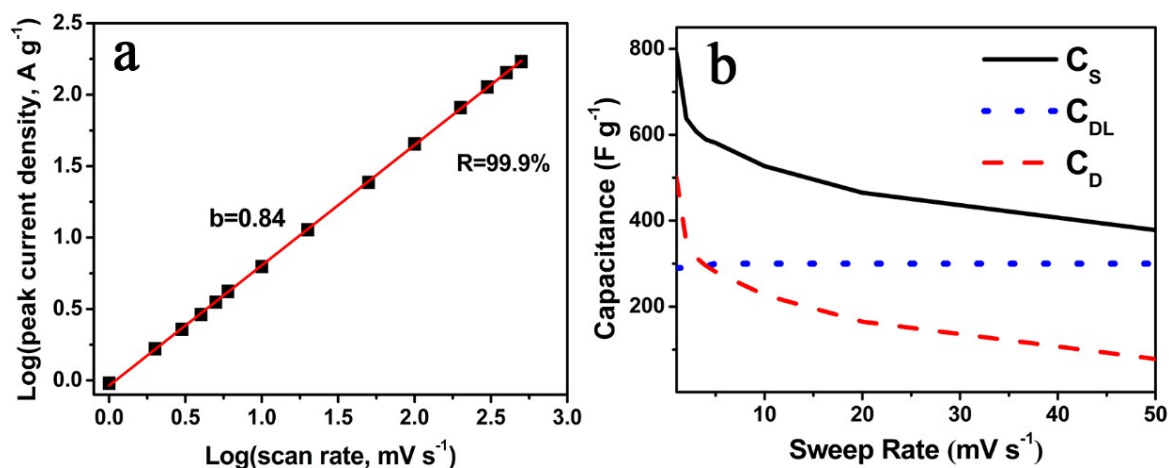


Fig. S7. (a) The b value and (b) contribution of diffusion- and surface-controlled process of the PPD- PMo_{12} @rGO aerogel electrode.

To further identify charge storage kinetics of the PPD- PMo_{12} @rGO aerogel electrode, the mathematical relationship between the log of peak current density (i) and the corresponding log of scan rate (v) was investigated according to equation: $i(v) = av^b$. The b value, as calculated from slope of $\log(v)$ - $\log(i)$ plots, of 0.5 and 1.0 indicates the capacitive contribution and the diffusion-controlled charge contribution, respectively. For the PPD- PMo_{12} @rGO aerogel electrode, the $\log(v)$ - $\log(i)$ plot is quasi-linear with b value close to 1 ($b = 0.84$) from 1 to 500 mV s^{-1} (Fig. S7a), indicating a main contribution from EDLC. In addition, the specific capacitance (C_s), the electrical double layer capacitance (C_{DL}) and the diffusion-controlled capacitance (C_D) for the aerogel electrode were calculated according to equation:

$$i(V) = k_1 v + k_2 v^{0.5} \quad (4)$$

where V is the potential, k_1 and k_2 are constants at different scan rates (See Experimental section for calculation details), and the results are presented in Fig. S7b. It can be seen that the C_{DL} was almost unchanged over the full range of scan rates, suggesting that the EDLC charge process is saturated. Fig. S7b also shows that the C_D decreased with the increasing scan rate. As a result, the C_D and C_{DL} makes dominated contributions to the C_S at low ($< 4 \text{ mV s}^{-1}$) and high scan rates ($> 4 \text{ mV s}^{-1}$), respectively. The reason might be that the electrolyte ions can well diffuse through the porous electrode materials at low scan rate. However, as the scan rate increases, the rate of ion diffusion was limited and thus led to a lower diffusive capacitance.¹⁸

Table S5 Comparison of capacitive performances of graphene-based electrode materials tested in three-electrode system. (Electrolyte: H₂SO₄)

No.	Samples	C _s (F g ⁻¹)	Cycling stability	Ref.
1	PMO ₁₂ O ₄₀ /PIL ^{a)} /rGO	408 (0.5 A g ⁻¹)	2000 cycles 98%	[19]
2	MoO ₃ /rGO	617 (1 A g ⁻¹)	6000 cycles 87.5%	[20]
3	Fe ₂ O ₃ /rGO	869 (1 A g ⁻¹)	5000 cycles 100%	[9]
4	CDs/PPy/GO	576 (0.5 A g ⁻¹)	5000 cycles 92.9%	[21]
5	S-g-A ^{b)} /rGO	767 (0.5 A g ⁻¹)	5000 cycles 92%	[22]
6	PANI hydrogel	636 (1 A g ⁻¹)	10000 cycles 83%	[23]
7	PNIPAM ^{c)} /rGO	292 (1 A g ⁻¹)	10000 cycles 96%	[24]
8	PANI/IL ^{d)} /rGO	662 (1 A g ⁻¹)	5000 cycles 93.1%	[25]
9	PANI/rGO aerogel	550 (1 A g ⁻¹)	1000 cycles 75%	[26]
10	Mn ₃ O ₄ @rGO	284 (2 mV s ⁻¹)	10000 cycles 80%	[27]
11	C-MOF@rGO	390 (1 mV s ⁻¹)	5000 cycles 97.8%	[28]
12	Ti ₃ C ₂ +Mo ₆ S ₈	1159 (1 mV s ⁻¹)	1500 cycles 99%	[29]
13	Ti ₃ C ₂ T _x /PAN@rGO	275 (5 mV s ⁻¹)	20000 cycles 88.4%	[30]
14	PPD-PMo₁₂@rGO aerogel	790 (1 mV s⁻¹)	30000 cycles 90.5%	This work

^{a)} PIL: Polymeric Ionic Liquid; ^{b)} S-g-A: Poly(styrenesulfonic acid-graft-polyaniline)

^{c)} PNIPAM: Poly(N-isopropylacrylamide); ^{d)} IL: Ionic Liquid

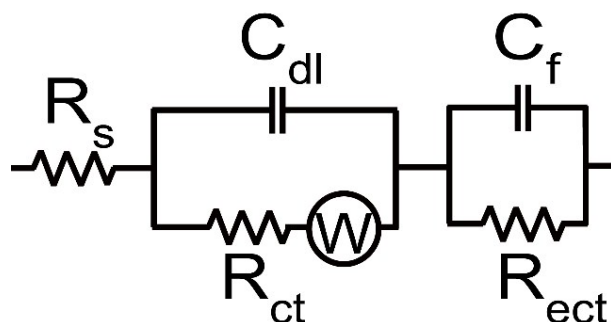


Fig. S8. The equivalent circuit of the PPD-PMo₁₂@rGO aerogel electrode.

Equivalent circuit used to extract various impedance components from the Nyquist plots consists of an equivalent series resistance (R_s) accounting for a combination of the electrolytic resistance, the internal resistance of the composite electrode and the contact resistance between the electrode and the current collector; a double-layer capacitor C_{dl} standing for the double layers formed on the surfaces of the electrode in contact with the electrolyte; a finite-length Warburg diffusion element Z_w resulted from the frequency dependence of ionic diffusion/transport in the electrolyte and to the surface of the electrode; an electrode-electrolyte interfacial charge transfer resistance R_{ct} ; a Faradaic pseudocapacitor C_f representing pseudocapacitance generated from the Faradaic redox reactions of the electrode material; and a reaction electron transfer resistor R_{ect} involved in the redox reactions. The C_{dl} in parallel with a serial combination of Z_w and R_{ct} forms composite interfacial impedance, which is then in series with the R_s and the overall redox reaction impedance that consists of the C_f in parallel with R_{ect} , making up the whole equivalent circuit. Simulated values were 0.486 Ω for the R_s and 0.481 Ω for the R_{ct} of the PPD-PMo₁₂@rGO aerogel electrode, which can also be suggested by the intercept on real impedance axis and the radius of the semicircle, respectively. The simulated values for R_s of PPD-PMo₁₂, PMo₁₂@GO, p-PD@GO and GO

were 0.62, 0.476, 0.487 and 0.34 Ω , respectively. In addition, the simulated R_{ct} values for these four samples were 0.59, 0.069, 0.82 and 0.256 Ω , respectively.

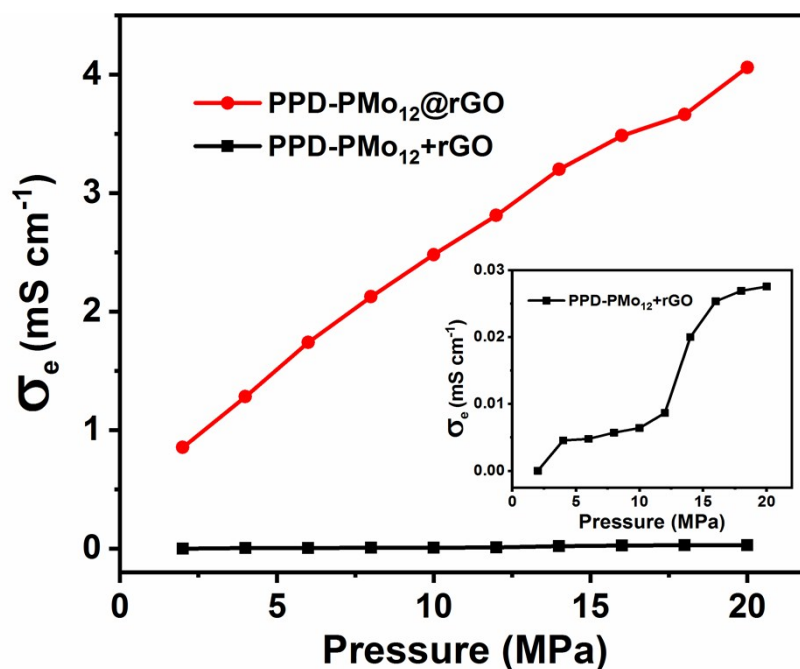


Fig. S9 Pressure dependence of electronic conductivity (σ_e) of the PPD-PMo₁₂@rGO aerogel (red line) and PPD-PMo₁₂+rGO (black line and the inset).

The electronic conductivity (σ_e) of PPD-PMo₁₂@rGO aerogel and PPD-PMo₁₂+rGO under different pressure measured from a ST2255 type high resistance meter with ST2722-SD model was presented in Fig. S9. The σ_e of both materials increases with increasing pressure. For PPD-PMo₁₂@rGO aerogel, a high σ_e of 0.85 mS cm⁻¹ and 4.06 mS cm⁻¹ was observed at 2 MPa and 20 MPa, respectively. On the contrary, the σ_e of PPD-PMo₁₂+rGO was only 8.8 × 10⁻⁶ mS cm⁻¹ at 2 MPa and 0.028 mS cm⁻¹ at 20 MPa, about 2-5 orders of magnitude lower than that of the PPD-PMo₁₂@rGO aerogel. These results indicate that the PPD-PMo₁₂@rGO aerogel has much better electron transfer ability than PPD-PMo₁₂+rGO, which

may be ascribed to the in-situ formed covalently linked dual net work structure of the PPD-PMo₁₂@rGO aerogel.

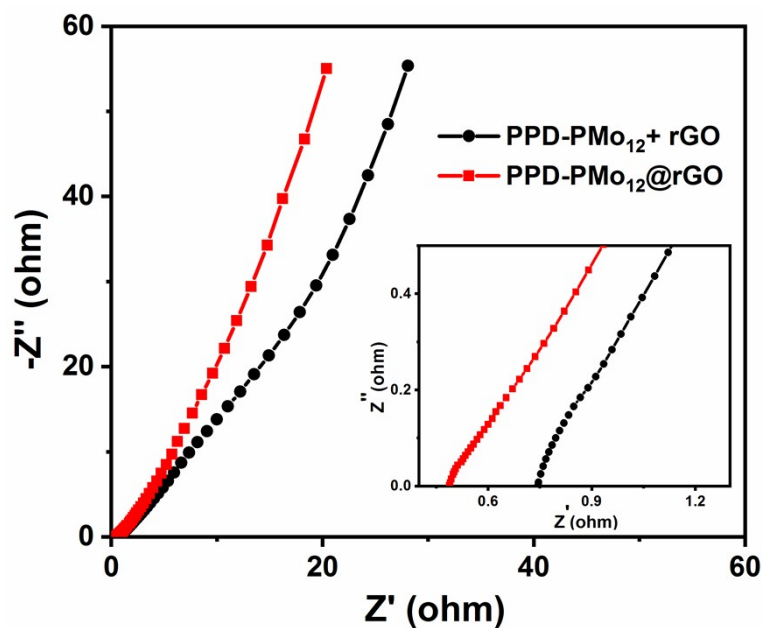


Fig. S10 Nyquist plots of PPD-PMo₁₂@rGO and PPD-PMo₁₂+rGO. The inset shows the expanded high-frequency region of the plots.

Electrochemical impedance spectroscopy (EIS) for PPD-PMo₁₂@rGO and PPD-PMo₁₂+rGO were tested in three-electrode system and the results are presented in Fig. S9. From the Nyquist plot of PPD-PMo₁₂+rGO (black line in Fig. S10), its simulated values of equivalent series resistance (R_s) and interfacial charge transfer resistance (R_{ct}) are 0.79 and 0.5 Ω , respectively. Both values are higher than those of PPD-PMo₁₂@rGO (0.486 Ω for R_s and 0.481 Ω for R_{ct}). Fig. 3d in manuscript shows the dependence of phase angle on the frequency for PPD-PMo₁₂@rGO and PPD-PMo₁₂+rGO, which has phase angle around -64.9° and -69.7° in the low frequency region, respectively, suggesting a charge storage mechanism

involving both electric double layer capacitance and pseudocapacitance. Besides, the characteristic frequency f_0 at a phase angle of -45° for PPD-PMo₁₂@rGO and PPD-PMo₁₂+rGO is 4.67 and 1.48 Hz, respectively, corresponding to a time constant τ_0 ($= 1/f_0$) of 0.214 and 0.675 s, respectively. The much shorter τ_0 of PPD-PMo₁₂@rGO indicates it has significantly enhanced ion transport rate compared to that of PPD-PMo₁₂+rGO.

References

- [1] Y. Xu, H. Bai, G. Lu, C. Li and G. Shi, *J. Am. Chem. Soc.*, 2008, **130**, 5856-5857.
- [2] P. Delahay and G. Perkins, *The Journal of Physical Chemistry*, 1951, **55**, 586-591.
- [3] S. Srinivasan and E. Gileadi, *Electrochim. Acta*, 1966, **11**, 321-335.
- [4] T. Brezesinski and J. Wang, S.H. Tolbert and B. Dunn, *Nat. Mater.*, 2016, **9**, 146.
- [5] V. Augustyn, J. Come, M.A. Lowe, J.W. Kim, P.L. Taberna, S.H. Tolbert, H.D. Abruña, P. Simon and B. Dunn, *Nat. Mater.*, 2013, **12**, 518.
- [6] B.K. Lesel, J.S. Ko, B. Dunn and S.H. Tolbert, *ACS Nano*, 2016, **10**, 7572-7581.
- [7] X. He, F. Zhang, J. Liu, G. Fang and S. Wang, *Nanoscale*, 2017, **9**, 18066-18074.
- [8] H. Bai, C. Li, X. Wang and G. Shi, *Chem. Commun.*, 2010, **46**, 2376-2378.
- [9] X. Xu, W. Shi, P. Li, S. Ye, C. Ye, H. Ye, T. Lu, A. Zheng, J. Zhu, L. Xu, M. Zhong and X. Cao, *Chem. Mater.*, 2017, **29**, 6058-6065.
- [10] R. Sun, H. Chen, Q. Li, Q. Song and X. Zhang, *Nanoscale*, 2014, **6**, 12912-12920.

- [11] Y. Jiang, H. Shao, C. Li, T. Xu, Y. Zhao, G. Shi, L. Jiang and L. Qu, *Adv. Mater.*, 2016, **28**, 10287-10292.
- [12] G. Yilmaz, X. Lu and G.W. Ho, *Nanoscale*, 2017, **9**, 802-811.
- [13] P. Li, Z. Jin, L. Peng, F. Zhao, D. Xiao, Y. Jin and G. Yu, *Adv. Mater.*, 2018, **30**, 1800124.
- [14] N. Ormategui, A. Veloso, G.P. Leal, S. Rodriguez-Couto and R. Tomovska, *ACS Appl. Mater. Interfaces*, 2015, **7**, 14104-14112.
- [15] A. Bora, K. Mohan, S. Doley and S.K. Dolui, *ACS Appl. Mater. Interfaces*, 2018, **10**, 7996-8009.
- [16] J.F. Wu, Q.E. Zhang, J.J. Wang, X.P. Huang and H. Bai, *Energy Environ. Sci.*, 2018, **11**, 1280-1286.
- [17] J. Li, G. Zhang, C. Fu, L. Deng, R. Sun and C.P. Wong, *J. Power Sources*, 2017, **345**, 146-155.
- [18] M. Forghani and S.W. Donne, *J. Electrochem. Soc.*, 2018, **165**, A664-A673.
- [19] M. Yang, B.G. Choi, S.C. Jung, Y.K. Han, Y.S. Huh and S.B. Lee, *Adv. Funct. Mater.*, 2014, **24**, 7301-7309.
- [20] X. Cao, B. Zheng, W. Shi, J. Yang, Z. Fan, Z. Luo, X. Rui, B. Chen, Q. Yan and H. Zhang, *Adv. Mater.*, 2015, **27**, 4695-4701.
- [21] X. Zhang, J.M. Wang, J. Liu, J. Wu, H. Chen and H. Bi, *Carbon*, 2017, **115**, 134-146.
- [22] J.W. Lee, J.U. Lee, J.W. Jo, S. Bae, K.T. Kim and W.H. Jo, *Carbon*, 2016, **105**, 191-198.
- [23] K. Zhou, Y. He, Q. Xu, Q.e. Zhang, A.a. Zhou, Z. Lu, L. K. Yang, Y. Jiang, D. Ge, X.Y. Liu and H. Bai, *ACS Nano*, 2018, **12**, 5888-5894.

- [24] R. Zhao, K. Li, R. Liu, M. Sarfraz and I. Shakir, Y. Xu, *J. Mater. Chem. A*, 2017, **5**, 19098-19106.
- [25] K. Halab Shaeli Iessa, Y. Zhang, G. Zhang, F. Xiao and S. Wang, *J. Power Sources*, 2016, **302**, 92-97.
- [26] R. Li, Y. Yang, D. Wu, K. Li, Y. Qin, Y. Tao and Y. Kong, *Chem. Commun.*, 2019, **55**, 1738-1741.
- [27] R. Sahoo, D.T. Pham, T.H. Lee, T.H.T. Luu, J. Seok and Y.H. Lee, *ACS Nano*, 2018, **12**, 8494-8505.
- [28] T. Van Ngo, M. Moussa, T.T. Tung, C. Coghlan and D. Losic, *Electrochim. Acta*, 2020, **329**, 135104.
- [29] F. Malchik, N. Shpigel, M.D. Levi, T.S. Mathis, A. Mor, Y. Gogotsi and D. Aurbach, *J. Mater. Chem. A*, 2019, **7**, 19761-19773.
- [30] M. Boota and Y. Gogotsi, *Adv. Energy Mater.*, 2019, **9**, 1802917.